Peer reviewed version

License (if available):
CC BY-NC-ND

Link to published version (if available):
10.1016/j.ijfatigue.2017.10.008

Link to publication record in Explore Bristol Research
PDF-document

University of Bristol - Explore Bristol Research
General rights

An experimental and numerical study on fatigue damage development in laminates containing embedded wrinkle defects

Supratik Mukhopadhyay*, Oliver J. Nixon-Pearson, Stephen R. Hallett

University of Bristol, Advanced Composites Centre for Innovation and Science, Queens Building, Bristol BS8 1TR, United Kingdom

*Corresponding author. Email: s.mukhopadhyay@bristol.ac.uk Tel: +44(0)1173315506

Abstract

Out-of-plane fibre waviness or 'wrinkle' defects significantly reduce the strength of laminated composites under quasi-static tension loads. Under tension-tension cyclic loading, the peak load amplitude remains lower than the wrinkled laminate quasi-static strength. Small delaminations can however still initiate early during the load history and grow steadily with increasing numbers of cycles until becoming critical, leading to ultimate structural failure. This paper focusses on the application of a novel 3D finite element modelling framework to predict fatigue delamination initiation and growth from wrinkle defects. An experimental programme was conducted alongside the modelling, for validation purposes. Carbon fibre/epoxy laminates with a quasi-isotropic layup containing artificially induced wrinkles were tested at various load severities (percentage of quasi-static failure load), until failure (defined percentage loss of the initial undamaged stiffness). Failure progression was closely monitored throughout the test. A detailed comparison between the novel finite element analyses and experiments was undertaken, and it was shown that the delamination locations, extent and cycles to failure could be very accurately predicted.

1

1   Introduction

In the last few decades fibre reinforced polymer composites have gradually been replacing metals as the material of choice for structural aircraft applications. These materials provide many advantages over traditional metals such as weight saving, stiffness and strength tailoring, high structural damping, better corrosion resistance etc. However, composite materials technology is a relatively new area of research and as such, does not benefit from the well-established design guidelines and manufacturing techniques that are otherwise available for metals. Manufacturing of composite components largely depends upon hand-laying of prepreg sheets on complex moulds, which means that manufacturing variations in finished components can occur. Variations from the nominal geometric or functional specifications that negatively affect the finished component quality are known as manufacturing induced defects [1]. Out-of-plane fibre waviness or 'wrinkling' is a defect type where fibres deviate from their ideal straight line path and show up in the form of a localised wave in the out-of-plane/thickness direction (Figure 1(a)). The severity of a wrinkle is characterised either by the wavelength λ and amplitude δ [2], or by the angle formed between the fibres in the wrinkle and a nominally straight fibre, known as the wrinkle angle θ [3] (Figure 1(b)).

Under quasi-static tension, wrinkle defects initiate early delamination in the wavy plies, causing failure [4–7]. For example, in [7], the authors noted a tensile strength reduction of ~23% in a quasi-isotropic laminate containing an embedded wrinkle ($\theta = 12.1°$) located centrally along the gauge length. Modelling studies confirmed the presence of high-through-thickness shear stresses in the wavy plies, which initiated the delamination failure.

Because many aircraft components are subjected to cyclic loads, and the presence of wrinkle defects in them cannot be ruled out completely, it is important to investigate delamination initiation and growth from a wrinkle under fatigue. The last few decades have seen a

considerable amount of research devoted to understand delamination fatigue, see for example, a comprehensive review by Martin [8]. Several numerical tools have also been developed to accurately predict fatigue delamination growth e.g. Turon *et al*.[9], Harper and Hallett [10], Kawashita and Hallett [11]. Very few studies have however looked into fatigue delamination originating from wrinkles. A notable work is due to Nikishkov *et al*. [12], where the authors proposed a progressive fatigue damage algorithm in a 3D finite element framework, which was subsequently applied to predict delamination and matrix crack onset and growth in a multidirectional laminate containing wrinkle defects induced intentionally by terminating plies at certain locations and subject to cyclic tension loading. The constitutive law expressed the interfacial normal and shear strengths as a function of the elapsed cycles in the form of an experimentally obtained S-N curve. These relations were then put in a stress based failure initiation criterion to solve for the remaining number of cycles until damage initiated at the present stress state. Following initiation, complete element failure was simulated by reducing the stresses to zero in a small number of solution increments, which was identified by a convergence study. Once a few elements failed, the stresses were recalculated and the procedure was repeated with the remaining number of elements. The authors were able to predict the number of cycles to global failure accurately for three different wrinkle configurations. Also, the model predicted the ply terminations in the wrinkle as the delamination onset locations, which was confirmed in the tests by identifying peak strain locations in the DIC strain contours corresponding to ply delaminations.

By contrast to the above failure criterion based only on initiation stresses, an energy based Paris type law has been used in several fatigue finite element models to predict the propagation of delamination [9,13].One such model is that which has been developed over the years at the University of Bristol [10,11,14]. The objective of this paper is to apply and update this novel fatigue delamination cohesive constitutive law for predicting delamination

onset and growth from artificial wrinkle defects under tension-tension cyclic loading. To obtain data for validation of the models, experiments were first carried out at various load severities on wrinkle specimens as well as wrinkle-free, nominally flat, baseline specimens. In the finite element modelling a user-defined cohesive law is used to predict both matrix-crack growth within a ply and delamination growth between plies. A phenomenological damage initiation criterion [14] in fatigue is used and its influence on overall damage progression is shown. The model outcomes are compared with the experiments for delamination locations, extent and cycles to failure (defined as a certain percentage loss of initial undamaged stiffness). Finally general conclusions and suggestions for possible improvements of the present modelling framework are made.

2   Experimental programme

2.1   Wrinkle coupon manufacture

IM7/8552 pre-preg supplied by Hexcel composites was hand laid to make the quasi-isotropic $[+45_2/90_2/-45_2/0_2]_{3s}$ specimens. The material has a nominal cured ply thickness (CPT) of 0.125 mm. Two prepreg sheets were stacked together during the layup to increase the CPT to 0.25 mm. The 'doubled-up' prepreg sheets were then laid on top of each other following the specified stacking sequence to make a panel from which tensile test specimens could be extracted in sufficient numbers. The specimen dimensions were 250 mm$\times$30 mm$\times$6 mm with a gauge length of 150 mm after tabbing (Figure 2(a)). To induce the wrinkle defect artificially, the same technique, described in previous work [7] was used. Thin strips of 90 degree prepreg were added at specific locations throughout the laminate to enforce the out of plane movement of the plies during consolidation (Figure 2(b)). To compensate for the extra material added, small sections of one of each of the doubled up 90°plies were selectively removed opposite the added ply material. This method resulted in wrinkle formation without

4

using any pre-cured or foreign substance in the layup, which could lead to the generation of a weak interface causing premature delamination. The thickness and width of the narrow 90° strips could be varied to change the wrinkle severity in a controlled manner. For the present study, a specific configuration was chosen that resulted in a wrinkle severity with mean wrinkle angle of 7.5°. For this configuration (designated as wrinkle level#2 in [7]), quasi-static tension loading caused delamination at the wrinkle site, which is associated with a small drop in the load curve at ~82% of the ultimate failure load. Final catastrophic failure of the specimen is caused by fibre fracture in the gauge section. Also, to compare the failure performance with and without the wrinkle defects, pristine specimens (free from any wrinkle) of same layup and geometric dimensions were also manufactured. For both the wrinkle and pristine configurations, several panels were manufactured, each of which could provide, on an average 10-15 specimens for testing.

2.2   Fatigue testing

Three specimens from the pristine and wrinkle configurations were tested to failure quasi-statically using a servo-hydraulic Instron 1342 tensile testing machine with a 250 kN capacity. From the ultimate quasi-static failure load of the specimens, the peak fatigue amplitudes could then be calculated. This gives rise to the term 'fatigue severity' and is denoted as a percentage of the ultimate load. The pristine specimens failed at a mean cross-sectional stress of 724.8 MPa (CV 0.9%) under quasi-static loading, while for the wrinkled specimens, it was 694.8 MPa (CV 2.4%). The static tensile strength of pristine specimens is in excellent agreement with results previously published [7], and the strength of the wrinkle specimens is ~7% higher. This is believed to be due to the slight manufacturing variations between different batches of wrinkle specimens, due to which the mean wrinkle angle of the present batch was ~1.3° lower compared to [7], which resulted in a slightly higher static tensile strength.

The fatigue tests were performed in an Instron 8801 servo-hydraulic tensile testing machine with a 100kN capacity load cell (Figure 3). Tension-tension cyclic loading was applied with an R-ratio = 0.1. Fatigue tests were run at different load severities (70, 60, 50, 40 and 30%) until no noticeable stiffness loss was recorded. A limit of 10^6 cycles was used. If no noticeable loss in stiffness was recorded at the cycle limit, then this was defined as a runout. A loading frequency of 3Hz was used for 60% load severity and adjusted linearly for other load severities to keep the loading rate constant. At least three specimens were tested at a given load severity for statistical significance. The machine was controlled from an external LabVIEW® programme, which provided a sinusoidal load signal for the fatigue loading. The other purpose of the programme was to pause the machine at the peak of the load cycle after a regular interval of cycles (specified by the user) for 0.5 sec and to trigger a camera focussed on the specimen gauge section. This enabled visual monitoring of the delamination growth over the course of the test, with the delaminations being held open during the pause at peak load. A clip gauge extensometer was attached to the specimen gauge section to record the tensile strain. The stiffness E of the specimen was measured as

$$E = \frac{(F_{max} - F_{min})}{A(\varepsilon_{max} - \varepsilon_{min})} \tag{1}$$

where F_{max} and F_{min} are the maximum and minimum tensile load on the specimen in a cycle obtained as an output from the machine, ε_{max} and ε_{min} are the corresponding maximum and minimum tensile strain obtained from the extensometer, and the measured cross-sectional area is A.

During fatigue loading, the temperature of the specimen rises due to frictional sliding of the delaminated interfaces and also due to hysteresis loss from the resin. The temperature rise is known to have a negative effect on fatigue life of composites [15]. An infrared (IR) camera was therefore focussed on the specimen gauge section (Figure 3) to monitor the temperature

rise. This was found to never exceed 10˚C during any of the tests, which is negligibly small in relation to any possible adverse effects on the resin properties.

Finally, several tests were interrupted at certain stages of damage accumulation during fatigue cycling. Micro X-ray computed tomography (CT) scanning was performed to visualise the internal state of damage using a Nikon X-TH 225kV machine. Each specimen was clamped in the rotation stage and positioned between the source and the detector. The X-ray beam is emitted from the target penetrating through the specimen onto the 16 bit 2000 x 2000 pixel flat panel detector. Throughout the scan the specimen was rotated a full 360° whilst incrementally taking a series of radiographs. These 2D radiographs were then reconstructed using a filtered back projection reconstruction algorithm to produce a 3D volume of the object. The scanning voltage was 74 kV, the current was 276 µA and the exposure time for each radiograph was 500 ms. After testing, but prior to CT scanning, the specimens were soaked for two days in X-ray dye-penetrant consisting of 250g of zinc iodide, 80ml distilled water, 80 ml isopropyl alcohol and 1ml Triton X100 (a surfactant which reduces the surface tension of the solution) to enhance X-ray contrast. The CT scan data was post-processed in the VG studio max 2.2 and Avizo® 8.1 software packages. The grey scale values in the CT scan data corresponded to the local x-ray absorption within the scanned volume of the specimen, which were different for the damaged region (delamination/matrix cracks, highlighted by the penetrant solution) and undamaged region. Consequently, delaminations and matrix cracks could be segmented by defining certain thresholds around the appropriate greyscale values. Testing was not resumed after interrupted testing as the penetrant is known to affect crack growth [16].

2.3   Experimental results

2.3.1   Wrinkle specimens

The stiffness degradation (normalised with respect to the initial undamaged stiffness) with elapsed cycles is shown in Figure 4. A run-out (no failure) at 10^6 cycles was obtained for a 30% load severity. For all other severities, the slope of the normalised stiffness dropped noticeably after certain number of cycles. The camera images (Figure 5) showed that this drop was associated with delamination occurring at the wrinkle site. Furthermore, tests at 50% load severity were stopped just after the stiffness drop and CT scanned to identify the locations and extent of the damage. Delaminations across the entire specimen width, localised at the wrinkle, can be clearly identified, as shown in Figure 6. The failure criterion for the wrinkled specimens is considered as the initial stiffness drop of around 6-8%. This is followed by a more gradual decline in the stiffness towards catastrophic failure of the specimen (figure 4). It should be noted that for quasi-static tension tests on these specimens, the delamination at the wrinkle happened at ~85% of the ultimate failure load (ultimate failure was due to fibre fracture in the 0° plies post delamination). The mean fatigue life for various load severities recorded was: 70% - 87 cycles (29.03% CV), 60% - 965 cycles (68.16% CV), 50% - 6768 cycles (25.66% CV) and 40% - 181,302 cycles (39.18%CV).

2.3.2   Pristine specimens

In absence of any seeded wrinkle defect, a completely different failure mechanism was observed in the laminates. Normalised stiffness vs. cycles for a severity range 40-70% is shown in Figure 7, indicating a more gradual failure. Run-out was obtained at a severity of 40% as shown. While the camera images could only show ply delaminations developing in the gauge section (Figure 8), CT scan images of tests interrupted after 10% stiffness loss were more indicative, clearly showing delaminations emanating from the laminate edges (due to

locally high stresses around the edges), which propagates towards the interior (Figure 9) as cycling progressed. Because the damage progression was gradual and did not have a distinguishable damage event in the stiffness curve, the failure criterion is defined in this case as the number of cycles until a 10% stiffness degradation occured. This is also to ensure that there was an almost vertical slope in the stiffness curves for all specimens. The mean fatigue life as noted for these specimens: 70% - 2444 cycles (2.04% CV), 60% - 12,974 cycles (7.30% CV) and 50% - 132,927 cycles (4.01% CV).

The detrimental effect of the wrinkle is apparent. Under the same load severity, the presence of an embedded wrinkle of 7.5° wrinkle angle reduced the fatigue life by more than an order of magnitude compared to the defect-free specimens. This was due to the wrinkle induced delamination. The high shear stresses at the wrinkle dominated over the laminate free-edge stresses (causing delamination in pristine specimens). The higher CV of the fatigue life of the wrinkle specimens compared to the pristine ones is attributed to the slight variation of wrinkle angles from specimen to specimen, induced by the manual layup procedure.

3   Finite element modelling

3.1   *Meshing tool for fatigue analysis*

The simulations were undertaken in the explicit finite element solver LS-Dyna. Delaminations between plies and matrix cracking within a ply, as seen in the CT scan images, were the modes of failure included in the analysis. 8 node single integration point solid elements (type 1 in LS-Dyna) were used to model both the plies and cohesive elements. Delamination was simulated by inserting cohesive element layers of thickness 0.01 mm between each ply of different fibre orientation. Additionally, rows of cohesive elements of the same thickness, oriented along the fibre direction were inserted within each ply to simulate matrix cracking. Usually, such an approach results in non-matched mesh pattern in

each ply in a multidirectional laminate, and necessitates use of tied constraints at the ply

interfaces to hold the assembly together. However, the use of tied constrains increases the

computational time significantly. In this work a novel, fully automated meshing technique,

developed by Li *et al* [17] was used, which resulted in a fully contiguous mesh. The aim was

to create an in-plane ply mesh using a repetitive unit cell pattern, which allowed to insert

cohesive elements representing matrix cracks between ply elements along $\pm45°$ or $90°$

directions, while keeping the mesh pattern the same for all plies (Figure 10). To simplify the

model, no cohesive elements were inserted into the $0°$ plies as those plies were aligned with

the loading direction, and thus the chances of matrix crack formation were insignificant. A

FORTRAN90 subroutine built the model from input of the geometric dimensions of the

laminate and the wrinkle, the unit cell dimension, the cohesive element thickness and the

spacing between two parallel matrix cracks within a ply, and inserted cohesive elements

automatically between solid ply elements along the desired interfaces. The wrinkle profile

was realised in the mesh with a sinusoidal curve (see [7] for more details) with a given height

and wavelength, which were taken as the average of the height and wavelength data obtained

by measurement from microscopic images of the polished gauge section of the wrinkle

specimens. The local material orientation in the wrinkle was generated using the option

AOPT=3 available in LS-Dyna. This assigns the material axis 3 to be the same as the

midplane normal of the elements. The mesh was designed such that the element midplane

followed the waviness, giving the correct local direction 3. The direction 2 needed to be

specified by the user, which in this case was the global y axis $[0\ 1\ 0]^T$ for all the elements,

which was also along the width of the laminate. The direction 1 was then decided as a cross

product between 2 and 3 direction vectors. For off-axis plies, an additional parameter 'beta'

defined the angle of rotation of the coordinate system in degrees about material direction 3,

which in the present case was $45°$, $90°$ or $-45°$, depending on the ply orientation. To reduce

computation time, only the central 90 mm of the entire gauge section (150 mm) was modelled. For fatigue calculations, typically a finer mesh is required than for quasi-static analyses as the fatigue cohesive zone length tends to be smaller than the quasi-static cohesive zone length. The mesh shown in Figure 11, had a unit cell in-plane size of 1 mm, which resulted in an individual element size ~0.35 mm, and a total of 931,456 solid elements in the model, including both the ply and cohesive elements.

3.2 *Constitutive law for fatigue*

The cohesive formulation used for fatigue crack growth presented here follows from the crack-tip tracking approach of Kawashita and Hallett [11]. For completeness, a brief outline of the formulation is provided, and interested readers are referred to [11] for details. Interfacial stiffness degradation due to cyclic loading is introduced as an additional damage variable in the bilinear traction-separation based constitutive law (Figure 12(a)) for delamination analyses under quasi-static loading (see Jiang et al [18]). Before damage onset, a high penalty stiffness in the cohesive elements connects the adjoining ply elements. A quadratic stress interaction criterion is used to detect onset of cohesive damage:

$$\left(\frac{\langle\sigma_{\mathrm{I}}\rangle}{\sigma_{\mathrm{I}}^{max}}\right)^2 + \left(\frac{\sigma_{\mathrm{II}}}{\sigma_{\mathrm{II}}^{max}}\right)^2 = 1 \qquad (2)$$

where σ_{I} and σ_{II} are the interfacial tractions in mode I and mode II respectively, and the prefix 'max' indicates corresponding strength in those modes. The Macaulay bracket on mode I traction indicates that normal compression does not induce any damage. Under quasi-static loading (i.e. in absence of fatigue), the relative separation between the top and bottom surface of the cohesive element drives the damage to complete failure using a displacement based damage variable D_{s}:

$$D_{\mathrm{s}} = \max\left[0, \min\left\{1, \frac{\delta_{\mathrm{m}} - \delta_{\mathrm{m}}^{\mathrm{e}}}{\delta_{\mathrm{m}}^{\mathrm{f}} - \delta_{\mathrm{m}}^{\mathrm{e}}}\right\}\right] \tag{3}$$

where δ_{m} is the mixed mode relative separation between the cohesive element faces, the superscripts 'e' and 'f' represent the value at damage onset and complete failure respectively. Complete failure is reached when the critical energy release rate under mixed mode satisfies the following power law criterion:

$$\left(\frac{G_{\mathrm{I}}}{G_{\mathrm{Ic}}}\right)^{\alpha} + \left(\frac{G_{\mathrm{II}}}{G_{\mathrm{IIc}}}\right)^{\alpha} = 1 \tag{4}$$

where G_{I} and G_{II} are the energy release rates in mode I and mode II respectively, the subscript 'c' indicates their critical value. The exponent α is taken to be unity for simplicity, since it shows a good fit to experimental data for the current material system [19].

For cyclic loading, a 'cycle jump' strategy is used whereby the load is increased smoothly from zero to peak cyclic load and held constant (see Figure 13). A certain number of cycles are assumed to have elapsed per unit simulation time, based on a user-given cycle frequency 'f'. The energy release rate amplitude ΔG, which is the difference of energy release rates between the peak and trough load condition in a cycle, is given by:

$$\Delta G = G_{\mathrm{max}}\left(1 - R^2\right) \tag{5}$$

where G_{max} is the energy release rate at the peak of a cycle and R is the R-ratio. From equation (2)-(4), a mixed mode critical energy release rate G_{c} is obtained, following which a Paris law of the form given by Equation (6) is used to estimate crack growth rate $\Delta a/\Delta N$:

$$\frac{\Delta a}{\Delta N} = C\left(\frac{\Delta G}{G_{\mathrm{c}}}\right)^{m} \tag{6}$$

The mixed mode Paris law coefficient and exponent C and m are obtained from their corresponding experimentally measured pure mode values (C_I, m_I in mode I and C_{II}, m_{II} in mode II) using the scheme proposed by Russell and Street [20]:

$$\left. \begin{array}{l} C = \dfrac{G_I}{G_I + G_{II}} C_I + \dfrac{G_{II}}{G_I + G_{II}} C_{II} \\[2ex] m = \dfrac{G_I}{G_I + G_{II}} m_I + \dfrac{G_{II}}{G_I + G_{II}} m_{II} \end{array} \right\} \tag{7}$$

At an element level, the crack growth rate can be approximated as:

$$\frac{da}{dN} \approx \frac{L_e}{\Delta N_f} \Rightarrow \Delta N_f = \left(\frac{da}{dN} \right)^{-1} L_e \tag{8}$$

where ΔN_f is the number of cycles within which the current element must fail, and L_e is the effective element length in the direction of crack advancement. In the present implementation, L_e was taken to be the square root of the in-plane area of the cohesive elements for simplicity, since a relatively regular mesh has been used. Assuming a cohesive element at peak load has already accumulated a static damage D_s (see Equation (3)), it will require an additional amount 1-D_s in order to fail completely. At this point a fatigue damage variable D_f is introduced, whose rate of increase is given by:

$$\frac{dD_f}{dN} = \frac{(1 - D_s)}{\Delta N_f} \tag{9}$$

The cyclic rate can be converted to the rate with respect to simulation time using the user defined frequency f, and thus D_f is updated at every time increment Δt:

$$D_f^{t+\Delta t} = D_f^t + \frac{dD_f}{dN} \Delta N = D_f^t + \frac{dD_f}{dN} f \Delta t \tag{10}$$

The cohesive traction σ_m is now reduced linearly from its damage onset value σ_m^0 using the following scheme:

$$\sigma_{\mathrm{m}} = \sigma_{\mathrm{m}}^0 \left(1 - D_{\mathrm{t}}\right) \quad \text{where,}$$
$$D_{\mathrm{t}} = D_{\mathrm{s}} + D_{\mathrm{f}} \tag{11}$$

The resulting cohesive response including combined static and fatigue damage is shown in Figure 12(b). Although the above mentioned damage law can be readily applied, cohesive zone modelling does not take account of a sharp crack tip unlike classical fracture mechanics (on which the Paris law is based), but rather represents damage as an extended cohesive zone ahead of the failed elements. Thus, applying the damage law to all the elements in the cohesive zone causes faster overall damage growth and conservative estimates. In order to confine the fatigue damage only to the crack tip (instead of the entire cohesive zone), Kawashita et al [11] suggested an in-situ tracking of the moving damage front and selectively applied the fatigue law only to the damaged cohesive elements that belong to the crack tip. This requires each cohesive element to 'know' the damage status of its neighbouring elements and attributes a non-local character to the algorithm.

Another aspect of this formulation is the damage initiation criterion. For the original fatigue degradation law to be active, an element needs to accumulate some static damage D_{s} a priori. Although this condition is usually satisfied under high load severities, the same cannot be guaranteed for lower load severities, or in absence of any stress concentrations (such as the pristine specimens studied in this work) using the stress based initiation criterion (Equation (2)). In order to address this issue, the work of May and Hallett [14] on fatigue damage initiation is additionally included in the current formulation, whereby the static interfacial strengths $\sigma_{\mathrm{I\,max}}$ and $\sigma_{\mathrm{II\,max}}$ are degraded as a function of the elapsed cycles N by using equations of the following form:

$$\left.\begin{array}{l} \sigma_{\mathrm{I,fat}}^{\max} = \sigma_{\mathrm{I}}^{\max} \left(1 - a_{\mathrm{SN_I}} \log(N)\right) \\[2mm] \sigma_{\mathrm{II,fat}}^{\max} = \sigma_{\mathrm{II}}^{\max} \left(1 - a_{\mathrm{SN_{II}}} \log(N)\right) \end{array}\right\} \tag{12}$$

where $\sigma_{\mathrm{I,fat}}^{\mathrm{max}}$ and $\sigma_{\mathrm{II,fat}}^{\mathrm{max}}$ are the modified mode I and II strengths and $a_{\mathrm{SN_I}}$ and $a_{\mathrm{SN_{II}}}$ are the corresponding slopes, which are obtained experimentally. This scheme was only applied to elements that did not have any static damage at the start of the fatigue cycling. This ensured that all elements would eventually satisfy the stress initiation criterion (Equation (2)) at some point as the cyclic loading is continued, and fatigue damage could be applied to them. Although the interfacial strength was modified with increasing numbers of cycles, the critical energy release rate G_{c} being a material property, was kept unchanged. As a result, the static displacement to failure in the bilinear traction-separation law was increased as shown in Figure 14.

In the present implementation, the damage law was implemented as an LS-Dyna user material subroutine (UMAT), written in FORTRAN90, where a neighbour map was created internally as a common block array at the beginning of the simulation, which contained the element IDs of the four edge-sharing neighbour elements of each cohesive element. If any of the neighbouring elements had failed, the current element was identified as a crack tip (see Figure 15), provided it had already accumulated some static damage D_{s}. If a current element was statically damaged, but none of the neighbour elements failed, then a comparison was drawn between the mixed mode energy release rate of the current element and its neighbours. If the current element had the highest energy release rate among its neighbours, it was taken as a crack tip. The damage state and energy release rate of each element were also stored as common block variables in order to enable access from other elements. The models contained nearly a million elements and thus were run on multiple Central Processing Units (CPUs) for faster computation. However, in a parallel simulation, each individual CPU gets its own local copy of a specified common block, which can store and exchange information only for elements which are being processed by that particular CPU. In order to make sure each of such local common blocks all had the same global information at the end of an increment,

several Message Passing Interface (MPI) routines were used to efficiently exchange information between CPUs.

3.3 Model results and comparison with experiments

Thermo-elastic properties of IM7/8552 and the user cohesive material properties for fatigue damage are given in Table 1 and 2. Before load application, thermal residual stress development in the laminate was simulated by reducing the ambient temperature from 180˚C (final cure temperature) to 20˚C (room temperature) and holding it constant for the rest of the simulation. The load severities for the fatigue simulation were based on the quasi-static tensile strength predicted by the models. Under monotonic tension, a laminate was considered failed when axial stress in any of the 0˚ plies exceeded the fibre tensile strength. The pristine model failed at a cross-sectional stress of 723.6 MPa and the wrinkle at 675.2 MPa, both of which are in very good agreement with experiments (see Section 2.2). For fatigue analysis, the tensile load was ramped up using a smooth curve from zero to peak load (for a given load severity) and held constant while the cycle jump method was used within the formulation to realise the passage of cycles and simulation of interface damage. The user defined cycle frequency f was set at a value such that the simulations could be finished in reasonable time, whilst avoiding elevated values that could induce dynamic effects in the models due to rapid damage growth. In order to speed up calculations a selective mass scaling was used to a target time increment size of 10^{-5} sec, which was seen reasonable as it did not induce any noticeable dynamic effects. A typical finite element model of a wrinkle specimen containing 931,456 solid elements and 1,046,675 nodes took ~30 hours to finish while running parallel on 16 SandyBridge cores clocked at 2.6GHz and each containing 4GB RAM.

3.3.1 Failure prediction in wrinkle specimen

The stiffness (normalised by its initial undamaged value) vs. cycles graph obtained from the models is plotted in Figure 16. Similar to experiments, the rapid drop in stiffness after a certain number of cycles could be predicted across all the load severities except for 30%, where a run-out occurred after 10^6 cycles. The models were queried for the damage (delamination and cracks) location and extent after the stiffness drop and compared with CT scan images obtained from the experiments, showing an excellent match (Figure 17). In order to check for mesh dependency, a model of 50% load severity was run with two other mesh densities (Figure 18). The results showed that the baseline mesh (1 mm unit cell size) was sufficiently accurate. Fatigue life obtained from the model were: 70% -76 cycles, 60% - 879 cycles, 50% - 11,300 cycles and 40% - 104,500 cycles, which are in good agreement with experiments (see Section 2.3.1) The influence of the damage initiation model (equation 12) on failure was briefly studied. The model at 40% severity was used. The model was run with and without the damage initiation criterion to check its influence on fatigue life. When the interfacial strengths were kept at their unmodified static value, the fatigue life was 543,000 cycles, which is noticeably higher than the experimental mean for this load severity (181,302 cycles).

3.3.2 Failure prediction in pristine specimen

For the pristine specimens, no defect was present, and therefore delaminations propagating from the specimen edge caused a gradual failure, defined as a 10% loss in initial stiffness (see Section 2.3.2). The model predictions for stiffness vs. cycles are shown in Figure 19. In this case a 40% load severity gave a run-out, which is in agreement with experiments. The edge delaminations could be successfully captured by the model as seen in Figure 20, by comparing damaged locations between CT scan data obtained from experiments and failed

elements extracted from model, shortly after failure. The fatigue life obtained from the model are: 70% -750 cycles, 60% - 7,168 cycles and 50% - 98,400 cycles. The model predictions in this case are more conservative (when compared with experimental results in Section 2.3.2). In the absence of any major local stress concentration at the start of fatigue cycling in these models, the strength reduction scheme (Equation 12) was crucial to initiate delamination as cycles progressed. However keeping this scheme active throughout the entire model run was seen to eventually initiate damage in a large number of cohesive elements, causing faster failure compared to experiments. Nonetheless, the presence of the initiation criterion in the models was crucial. To give an example, a 40% load severity model run with the strength reduction scheme deactivated, didn't show any static delamination in the models at the beginning of the fatigue cycling, and thus would have predicted infinite fatigue life. Although, at this severity a run-out occurred at a million cycles, it did indeed suffer ~4% loss in stiffness at 10^6 cycles (and clearly had some damage, see Figure 9), and therefore would have failed eventually, if cycling was continued. With the strength reduction criterion active, the same model was able to predict ~7% loss in stiffness at the end of a million cycles. Although the fatigue life prediction was slightly conservative, the physical process of delamination growth with cycling could be correctly captured at this severity level. The mesh size sensitivity studies were also carried out for pristine specimens (not presented for brevity), and the baseline mesh (1 mm unit cell size) was found to be sufficiently accurate.

4   Discussion and Conclusion

The present work highlights the detrimental effect of wrinkle defects in causing early delamination onset under tension-tension fatigue loading and provides a robust and accurate finite element modelling framework to predict such failure. As part of this, a thorough study was undertaken, where laminates with an embedded wrinkle defect of a known severity were

manufactured and tested to failure. Defect-free pristine specimens are also tested in order to differentiate between the damage mechanisms with and without the presence of a wrinkle and to compare their failure performance. Figure 21 shows a summary of the experimental and numerical results plotted as S-N curves, where the severities for each of the cases (pristine and wrinkle) are expressed by normalising the applied peak cyclic stress to the static tensile strength in the respective cases. The experimental and numerical results are in excellent agreement with each other. The fatigue life of wrinkle specimens is approximately an order of magnitude lower than the pristine specimens for a given load severity, which, in addition to the knockdown in quasi-static properties, clearly demonstrates the negative impact of embedded wrinkles on high-cycle fatigue life of composite components. Another major contribution of this work is the development of a novel fatigue delamination modelling strategy in a cohesive element framework and its implementation in a commercial 3D finite element code. Unlike many existing fatigue modelling methods whose applicability has only been demonstrated on simple fracture coupons or in 2D, the present method is programmed to handle larger 3D structural models with complex cracking and delamination patterns, running in parallel environment and giving very accurate results. It is however acknowledged that the method still is limited to a ply-by-ply modelling approach and hence component scale models would be computationally expensive. In such a case a sub-modelling or multi-scale approach is recommended. The known limitation of stress based damage initiation criterion in cohesive elements to correctly predict initiation under low load severities is addressed by an experimentally obtained strength reduction model to further increase the models robustness. Lastly, this modelling method is very general and not only limited to predicting failure in a wrinkle, but in any general multi-directional laminate modelled using a ply-by-ply scheme. In future it may be possible to improvise on the fatigue initiation criterion, which

could provide less conservative predictions in the absence of pre-existing stress concentrations and under low load severities.

5   Acknowledgement

6   References

[1]   Potter KD. Understanding the origins of defects and variability in composites manufacture. 17 th Int. Conf. Compos. Mater., Edinburgh International Convention Centre, Edinburgh, UK: 2009, p. 27–31.

[2]   Adams DO, Hyer M. Effect of layer waviness on the compression strength of thermoplastic composite laminates. J Reinf Plast Compos 1993;12:414–29.

[3]   Potter KD, Khan B, Wisnom M, Bell T, Stevens J. Variability, fibre waviness and misalignment in the determination of the properties of composite materials and structures. Compos Part A Appl Sci Manuf 2008;39:1343–54.

[4]   El-Hajjar RF, Petersen DR. Gaussian function characterization of unnotched tension behavior in a carbon/epoxy composite containing localized fiber waviness. Compos Struct 2011;93:2400–8.

[5]   Makeev a., Seon G, Lee E. Failure Predictions for Carbon/Epoxy Tape Laminates with Wavy Plies. J Compos Mater 2009;44:95–112.

[6]   Bloom LD, Wang J, Potter KD. Damage progression and defect sensitivity: An experimental study of representative wrinkles in tension. Compos Part B Eng 2013;45:449–58.

[7]   Mukhopadhyay S, Jones MI, Hallett SR. Tensile failure of laminates containing an embedded wrinkle; numerical and experimental study. Compos Part A Appl Sci Manuf 2015;77:219–28.

[8]   Martin R. Fatigue in composites. Woodhead Publishing Ltd.; 2003.

[9]   Turon a., Costa J, Camanho PP, Dávila CG. Simulation of delamination in composites under high-cycle fatigue. Compos Part A Appl Sci Manuf 2007;38:2270–82.

[10]   Harper PW, Hallett SR. A fatigue degradation law for cohesive interface elements - Development and application to composite materials. Int J Fatigue 2010;32:1774–87.

[11]   Kawashita LF, Hallett SR. A crack tip tracking algorithm for cohesive interface element analysis of fatigue delamination propagation in composite materials. Int J

Solids Struct 2012;49:2898–913.

[12] Nikishkov Y, Makeev A, Seon G. Progressive fatigue damage simulation method for composites. Int J Fatigue 2013;48:266–79.

[13] Pirondi A, Moroni F. A Progressive Damage Model for the Prediction of Fatigue Crack Growth in Bonded Joints. J Adhes 2010;86:501–21.

[14] May M, Hallett SR. A combined model for initiation and propagation of damage under fatigue loading for cohesive interface elements. Compos Part A Appl Sci Manuf 2010;41:1787–96.

[15] Charalambous G, Allegri G, Hallett SR. Temperature effects on mixed mode I/II delamination under quasi-static and fatigue loading of a carbon/epoxy composite. Compos Part A Appl Sci Manuf 2015;77:75–86.

[16] Spearing SM, Beaumont PWR. Fatigue damage mechanics of composite materials. I: Experimental measurement of damage and post-fatigue properties. Compos Sci Technol 1992;44:159–68.

[17] Li X, Hallett SR, Wisnom MR. Modelling the effect of gaps and overlaps in automated fibre placement (AFP)-manufactured laminates. Sci Eng Compos Mater 2015;22:115–29.

[18] Jiang WG, Hallett SR, Green BG, Wisnom MR. A concise interface constitutive law for analysis of delamination and splitting in composite materials and its application to scaled notched tensile specimens. Int J Numer Methods Eng 2007;69:1982–95.

[19] Jimenez MA, Miravete A. Application of the Finite-Element Method to Predict the Onset of Delamination Growth. J Compos Mater 2004;38:1309–35.

[20] Russell A., Street K. Predicting interlaminar fatigue crack growth rates in compressively loaded laminates. In: Lagace P., editor. Compos. Mater. fatigue Fract., ASTM International; 1989, p. 162–78.

[21] May M. A new model for initiation of damage under fatigue loading for cohesive elements. University of Bristol, 2010.
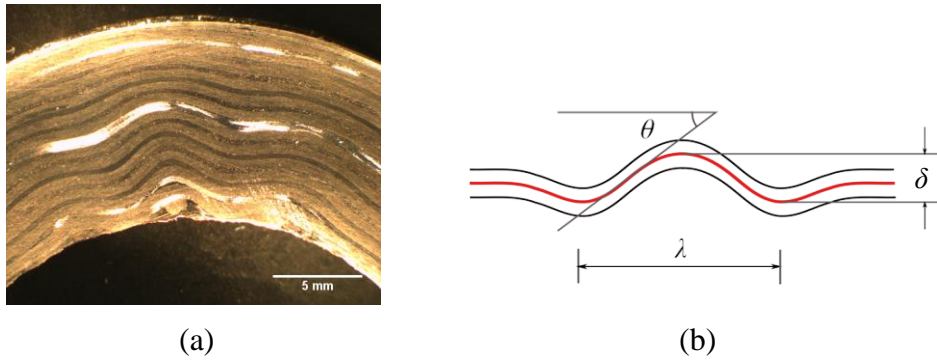
Figure 1. (a) Wrinkle formation in a curved composite part. (b) Geometric parameters defining the severity of a wrinkle defect.
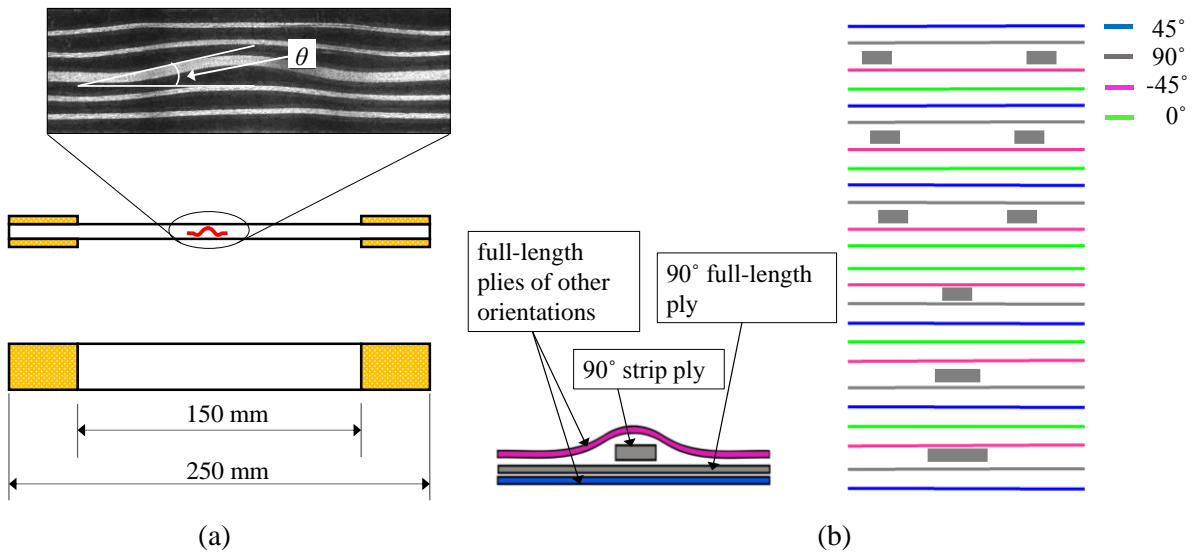
Figure 2. (a) Tensile specimen with artificial wrinkle in the middle of the gauge length (dimensions not to scale). (b) Method of inducing artificial wrinkle (left) and complete layup (right).
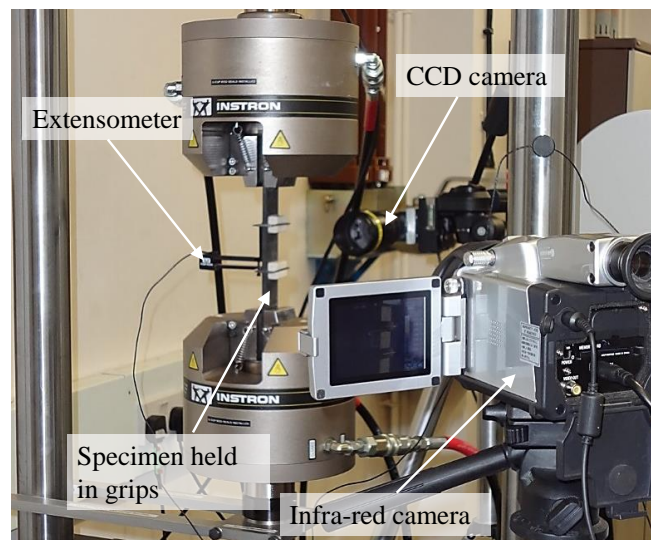
Figure 3. Experimental set-up
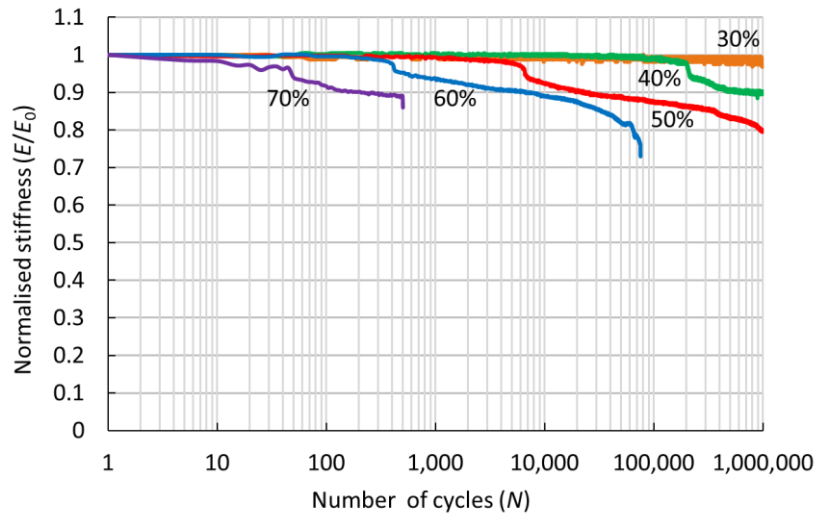
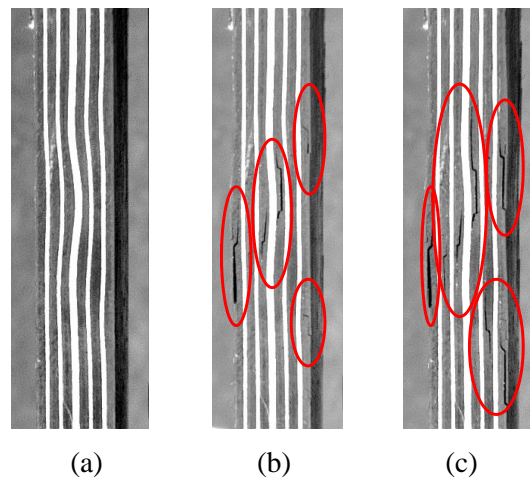**Figure 4**.Typical normalised stiffness vs. cycles graph of wrinkle specimens at different load severities

(a)   (b)   (c)

Figure 5. Camera images of damage evolution in the gauge section of a wrinkle specimen at 50% severity (highlighted in red circles) during test (a) 0 cycles (b) 4,000 cycles (c) 8,000 cycles.
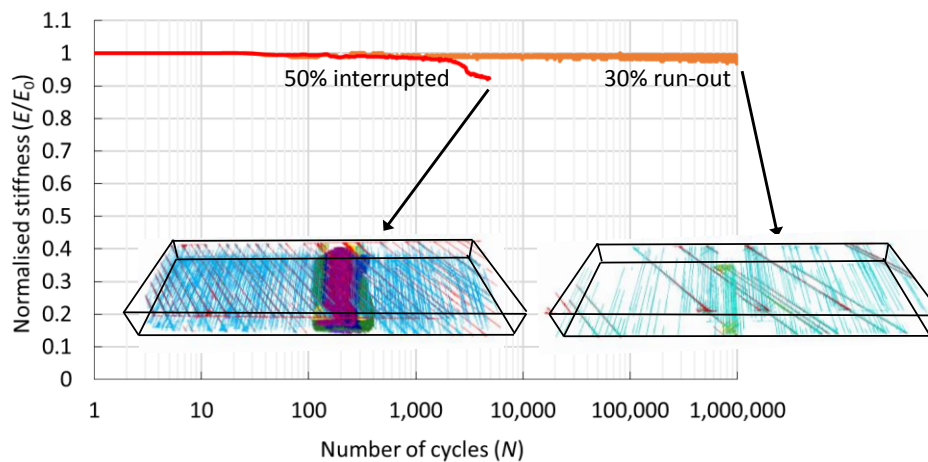
Figure 6. Post-processed CT scan images (cracks with different orientations and delaminations at different interfaces highlighted with different colours) of two wrinkle specimens, one run-out at 30% severity, showing no observable delamination, another at 50% severity interrupted after stiffness drop, showing extensive delamination at the wrinkle site.

23
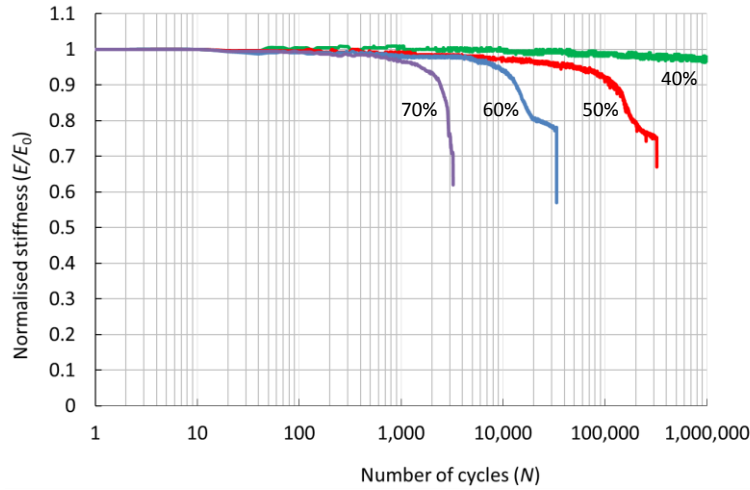
Figure 7.Normalised stiffness vs. cycles graph of pristine specimens at different load severities.

(a)   (b)   (c)
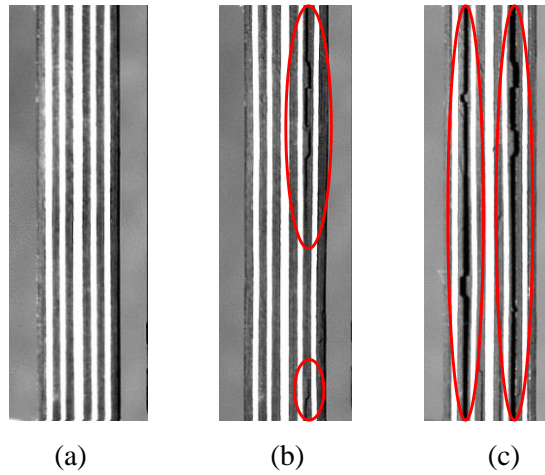
Figure 8. Camera images of damage evolution in the gauge section of a pristine specimen at 50% severity (highlighted in red circles) during test (a) 0 cycles (b) 100,000 cycles (c) 150,000 cycles.
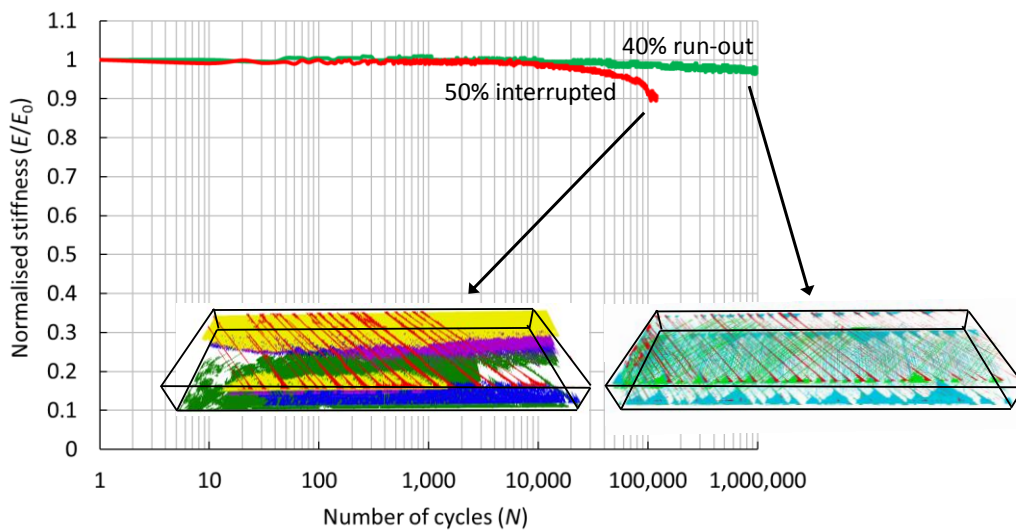
Figure 9. Post-processed CT scan images (cracks with different orientations and delaminations at different interfaces highlighted with different colours) of two pristine specimens, one run-out at 40% severity, showing many matrix cracks but no major delamination, another at 50% severity interrupted after 10% stiffness drop, showing significant delamination along the specimen edge.
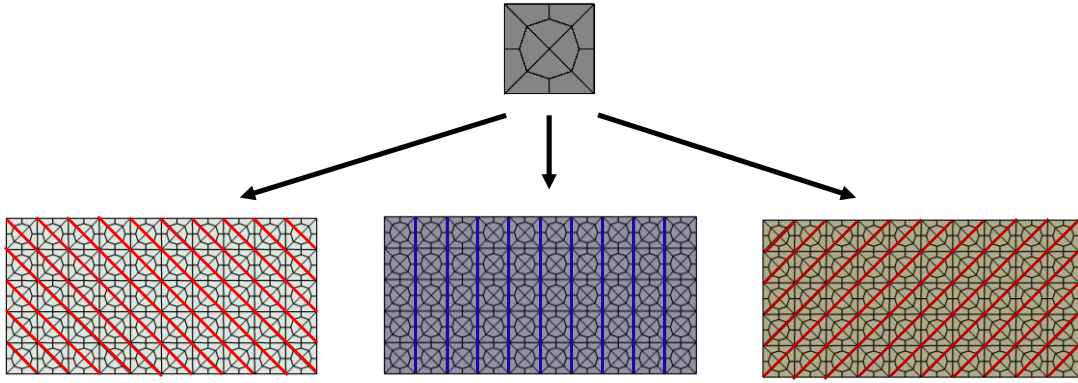
Figure 10. A unit cell pattern containing 12 solid elements (top) is repeated along specimen length and width direction to create each ply mesh. Possible locations for cohesive element insertion between solid elements to simulate matrix cracks is shown for -45° plies in red(bottom left), 90° plies in blue (bottom middle) and 45° plies in brown (bottom right).
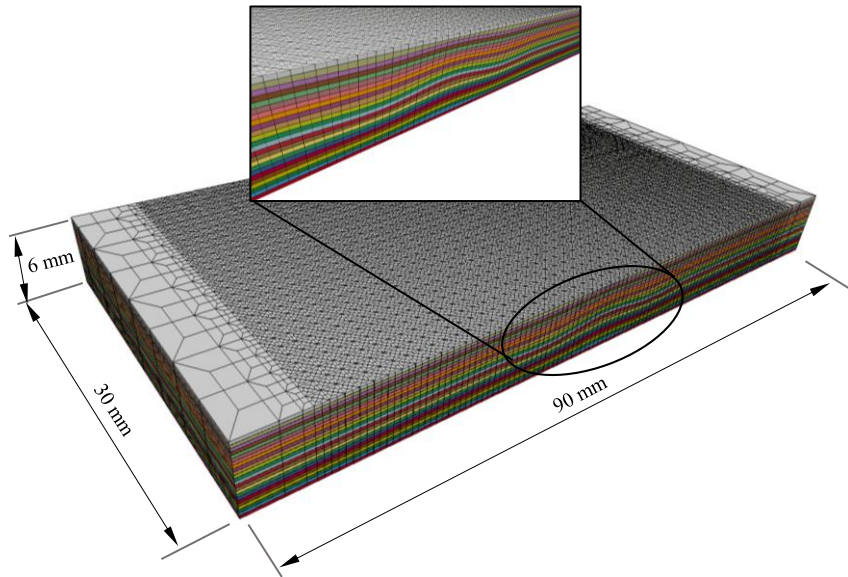
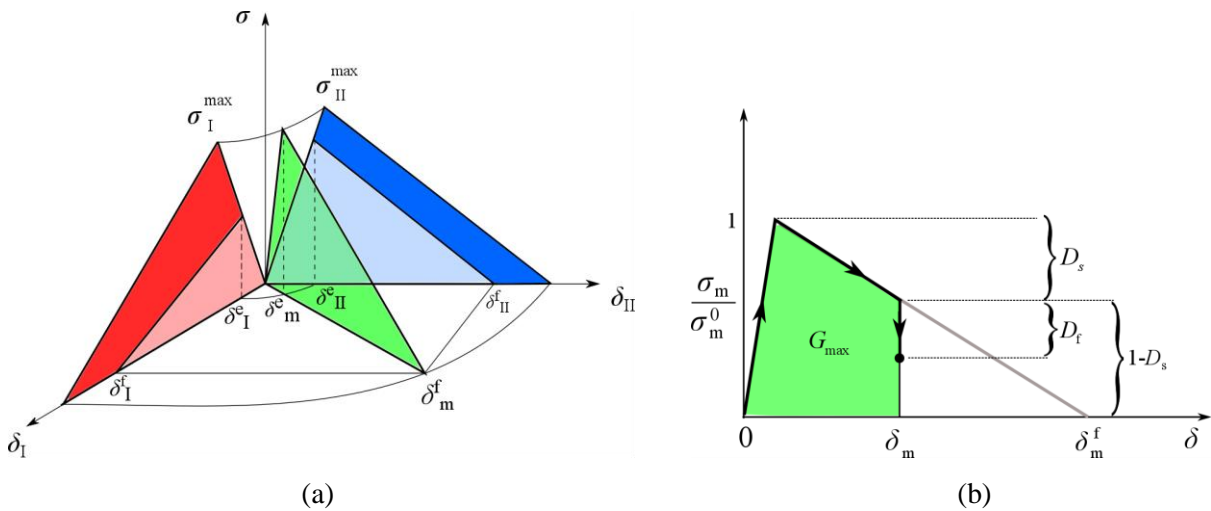**Figure 11**. Finite element mesh of the wrinkle specimen. A close-up view of the wrinkle is shown in the inset.

(a)   (b)

Figure 12. (a) Static mixed mode cohesive bilinear law, following [18]. (b) Fatigue cohesive law, following [11] (the loading path is highlighted).
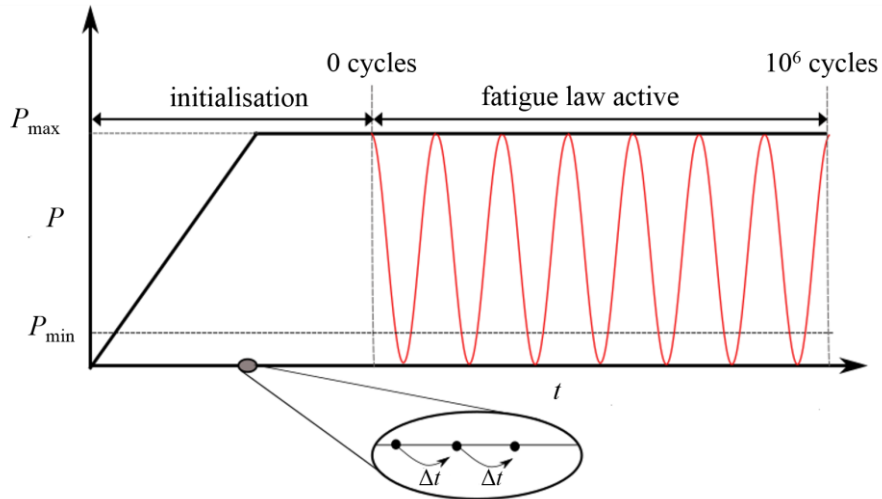
Figure 13. Cycle-jump strategy for simulation of high-cycle fatigue.
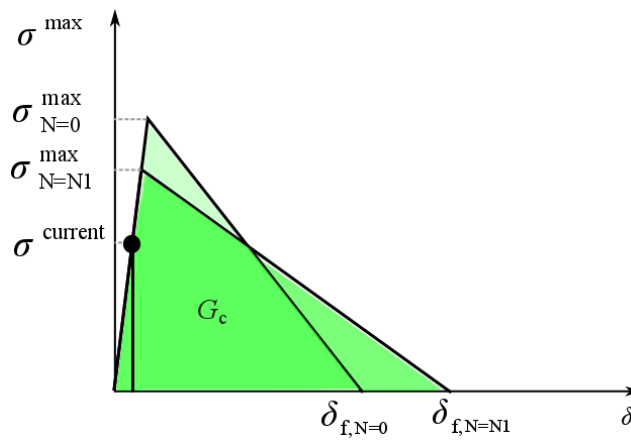
Figure 14. Cohesive strength reduction with cycles in the static bilinear law in order to initiate damage in an element which is presently elastically loaded under the peak fatigue load.
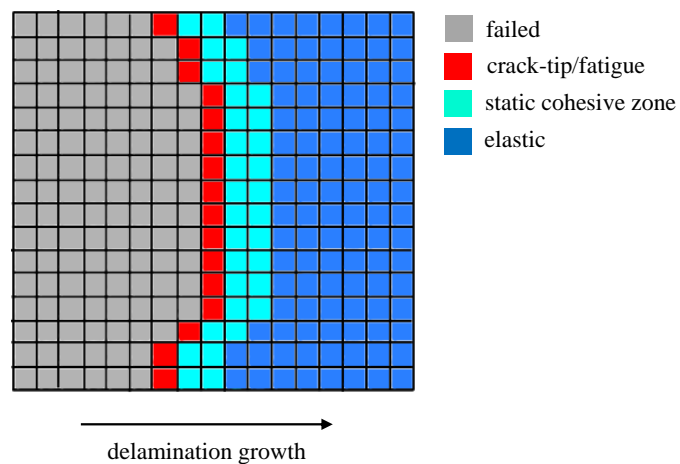

Figure 15. Approximating a sharp crack front as a single row of elements (red) adjacent to failed elements (grey) in its neighbourhood, using the crack-tip tracking approach [11]. The other elements in the cohesive zone (cyan) remain unaffected by fatigue.
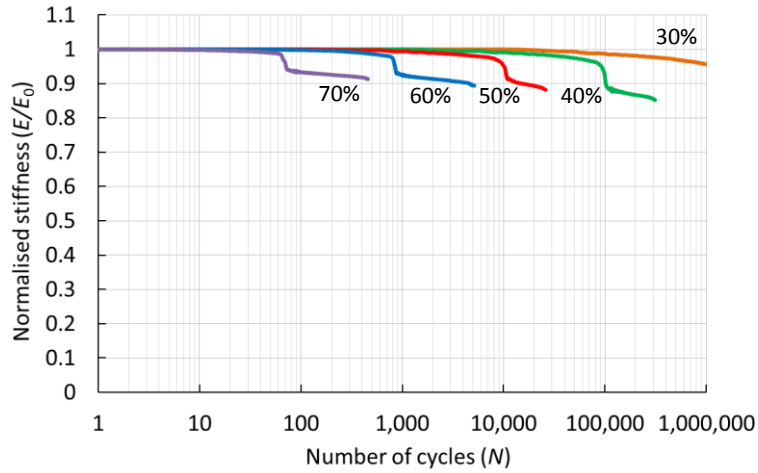
Figure 16. Simulation results of stiffness vs. cycles graph of wrinkle specimen at different load severities.
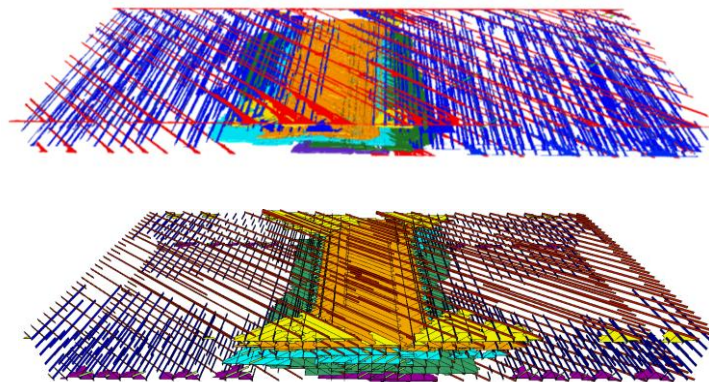

Figure 17. Delamination and crack locations and extent in a wrinkle specimen at 50% load severity shortly after failure (corresponding to the sharp drop in stiffness). Different ply interfaces and crack orientations are coloured differently for ease of identification: CT scan of experimental specimen (above) (b) Model results (below).
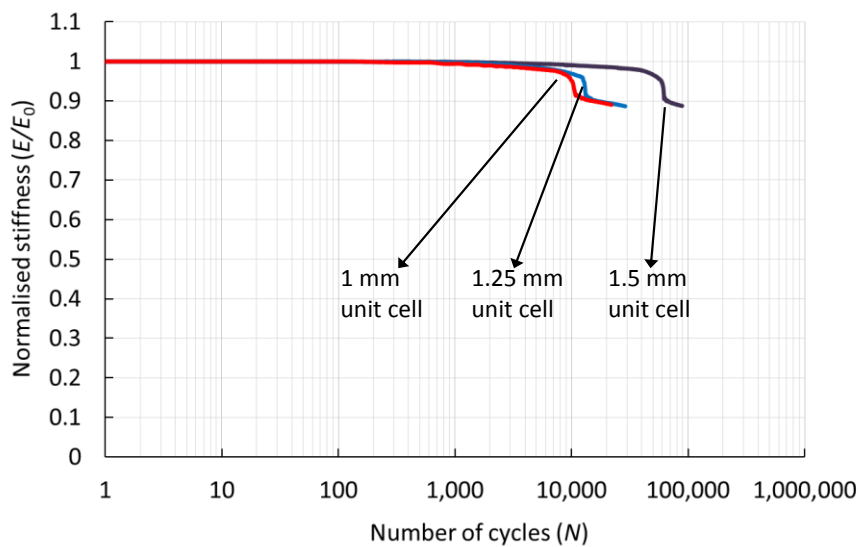

Figure 18. Mesh sensitivity study on a 50% load severity wrinkle specimen showing stiffness vs. cycles to failure for three different unit cell sizes.
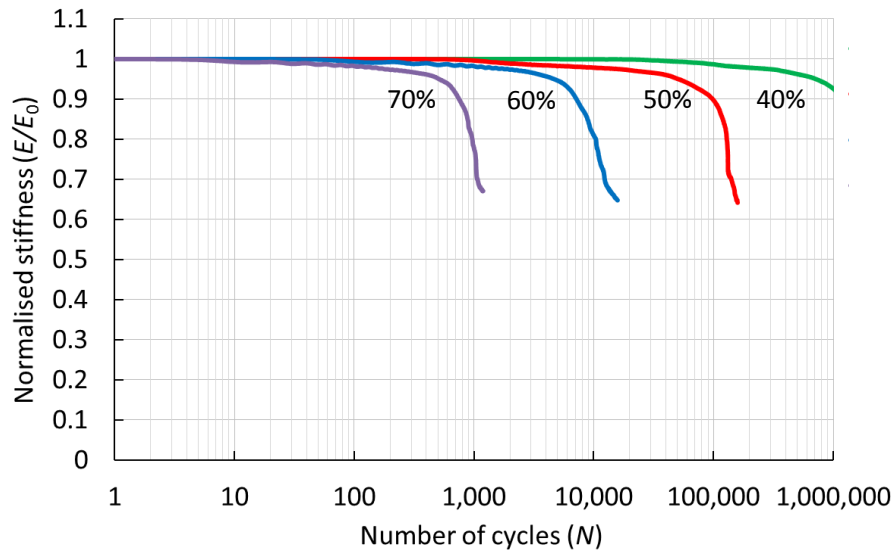
Figure 19. Simulation results of stiffness vs. cycles graph of pristine specimen at different load severities.
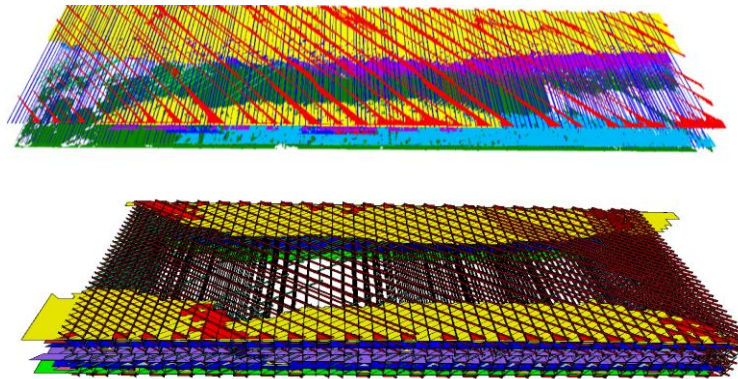

Figure 20. Delamination and crack locations and extent in a pristine specimen at 50% load severity shortly after failure Different ply interfaces and crack orientations are coloured differently for ease of identification: CT scan of experimental specimen (above) (b) Model results (below).
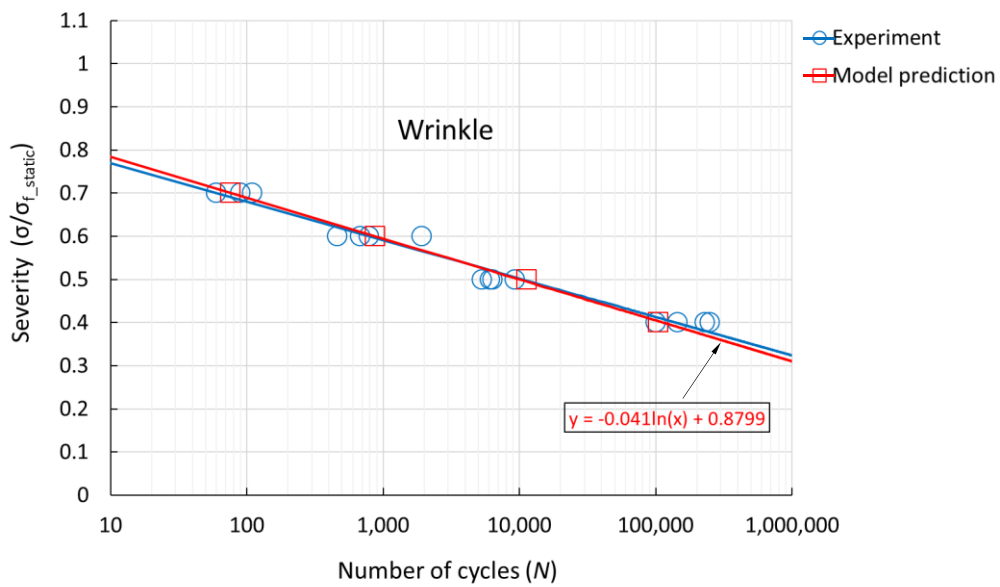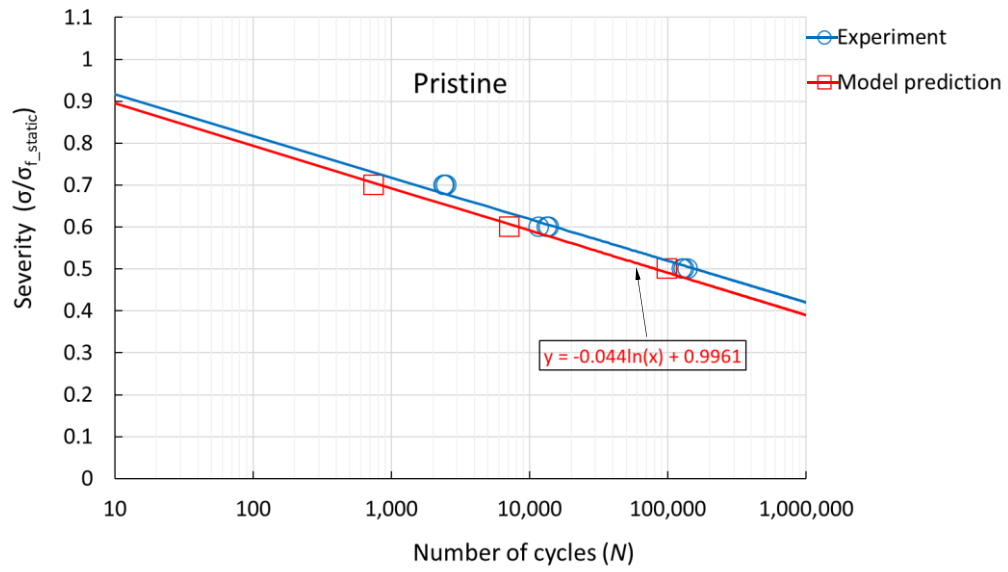
Figure21. Summary of the results plotted as S-N curves obtained from experiments (blue) and model (red), for pristine specimens (above) and wrinkle specimens (below).

Table 1. Thermo-elastic properties of IM7/8552[11]

E_{11} (MPa)	E_{22} (MPa)	E_{33} (MPa)	γ_{12}	γ_{13}	γ_{23}	G_{12} (MPa)	G_{13} (MPa)	G_{23} (MPa)	α_{11} (/°C)	α_{22} (/°C)	α_{33} (/°C)
161000	11380	11380	0.32	0.32	0.43	5170	5170	3980	0	3e-5	3e-5

Table 2. Cohesive interface properties of IM7/8552 for fatigue damage [18,21]

K_I (N/mm^3)	K_{II} (N/mm^3)	σ_I^{max} (MPa)	σ_{II}^{max} (MPa)	G_{Ic} (N/mm)	G_{IIc} (N/mm)	α
10^5	10^5	60	90	0.2	1.0	1
C_I (mm/cycle)	C_{II} (mm/cycle)	m_I	m_{II}	$a_{SN,I}$	$a_{SN,II}$	
0.00651	0.087	5.29	6.7071	0.072	0.071	